This is a repository copy of *Suppressing Auger Recombination of Perovskite Quantum Dots for Efficient Pure-Blue-Light-Emitting Diodes*.

White Rose Research Online URL for this paper:
https://eprints.whiterose.ac.uk/195460/

Version: Supplemental Material

Supporting Information

Suppressing Auger Recombination of Perovskite Quantum-Dot for Efficient Pure-Blue Light-Emitting Diodes

Chenghao Bi[1†], Zhiwei Yao[1†], Jingcong Hu[2†], Xingyu Wang[3], Mengqi Zhang[1], Shuyu Tian[1], Aqiang Liu[1], Yue Lu[2], Nora H. de Leeuw[3,4], Manling Sui[2], Jianjun Tian[1,5]*

[1] Institute for Advanced Materials and Technology, University of Science and Technology Beijing, 100083, China.
[2] Beijing Key Laboratory of Microstructure and Properties of Solids, Institute of Microstructure and Properties of Advanced Materials, Beijing University of Technology, Beijing 100124, China.
[3] School of Chemistry, University of Leeds, Leeds LS2 9JT, UK
[4] Department of Earth Sciences, Utrecht University, 3584 CB Utrecht, The Netherlands
[5] Shunde Innovation School, University of Science and Technology Beijing, 100083, China.

†These authors contributed equally to this work
*Corresponding author. E-mail: tianjianjun@mater.ustb.edu.cn

Experimental Section

Materials. Cesium carbonate (Cs_2CO_3, alfa 99.9%), oleylamine (OAm, Aladdin 90%), lead (II) bromide ($PbBr_2$ youxuan 99%), Zinc bromide ($ZnBr_2$ Aladdin 99%), phenylethylamine (PEA, Sigma-Aldrich 90%), 1-octadecene (ODE, alfa technical grade 90%), didodecylamine (DDDAM, TCI 97%), hydrogen bromide (HBr, Sigma-Aldrich), hexane (Aladdin analytical reagent 97%), methyl acetate (MeOAc, Aladdin anhydrous 99.5%), oleic acid (OA, Sigma-Aldrich analytical reagent 90%), ethyl acetate (Aladdin anhydrous 99.5%).

Preparations of Cs-oleate precursor. A three-necked flask with 0.1 g of Cs_2CO_3, 10 mL ODE with 0.8 mL OA was placed in heating agitator. The mixture solution was heated to 100 °C in vacuum for degassing. After heating for 1 h, the temperature was increased to 120 °C and continue heating for 1h. Then N_2 was pumped into flask and continue degassing for 20 min. The process was repeated 3 times to remove H_2O and O_2 completely. The clear Cs-Oleate solution was obtained, which was kept at 90 °C before using, otherwise it would solidify at room-temperature (<30°C).

Synthesis of blue-emitting $CsPbBr_3$ QDs (control QDs）. The synthesis of blue-emitting $CsPbBr_3$ QDs was followed our previous work. A 50 ml three-necked round flask with 10 ml ODE and 0.138 g $PbBr_2$ was placed in a heating agitator, which was heated to 100 °C in vacuum for degassing 1 h, then the temperature was increased to 120 °C and continue heating for 1 h. After that, the N_2 flow was pumped into flask, which was kept under flow constant. Then 0.6 ml OAm and 1.2 ml OA pre-heated at 70 °C were injected to the mixture solution. Then the mixture solution was degassed under vacuum until no bubbles were produced and then the N_2 flow was pumped into flask and the temperature was decreased to 90 °C. At this stage, 1.6 ml Cs-oleate precursor solution was quickly injected to the flask. After 10 seconds, 60 μL HBr was immediately injected to the mixture solution. Note: In order to minimize the effects of water, the purity of HBr should be as high as possible. After 10 seconds, the DDDAM in toluene was injected to the flask. Note: QDs are easy to be turbid after adding HBr, so the DDDAM should be added when mixture is about to become turbid. the flask was swiftly cooled by an ice bath. The $CsPbBr_3$ QDs were purified by mixing with MeOAc (volume ratio 2:1) and then centrifugation at 9000 rpm for 5 min. After the purification process, 10 μL PEA was mixed with 1 mL purified $CsPbBr_3$ in toluene colloidal solution to ligand exchange under stirring for

a few minutes. The final treated CsPbBr$_3$ QDs were separated by ethyl acetate and centrifugation, and then were redissolved in hexane. This cycle was repeated twice to three times, the final products were redispersed in octane.

Synthesis of Z-QDs. The synthesis of blue-emitting Z-QDs was all same as the process of QDs except that 0.425 g ZnBr$_2$, 4 mL OA and 4 mL OAm was placed in the Pb-oleate. For ligand exchange, ZnBr$_2$ was dissolved into ethyl acetate or ethanol to form Zn-Br saturated solution. Then, ~20 μL of Zn-Br ligand solution was added into 5 ml of purified CsPbBr$_3$ QD solution in toluene (intermediated QDs). After ~5 min vortexed or ultrasonication, the mixture was centrifuged at 8000 rpm for ~1 min to remove any insoluble solids. Adequate response is the key to success. Then, methyl acetate was added to the mixture to precipitate the Z-QDs. After centrifuging, the supernatant was discarded while the precipitate was re-suspended into octane.

Preparation of ZnO nanocrystals. 0.296 g ZnAc$_2$•2H$_2$O, 0.032g MgAc$_2$•4H$_2$O and 15 mL DMSO were added into flask and keep stirring to from clear mixed solution. Then, 0.343 g TMAH dissolved in 5 mL ethanol solution, and added into mixed solution, which reacted at 60 °C for 1 h. The precipitates were purified with methanol several times and then redispersed in ethanol/isopropanol solution (~25 mg/ml).

Device fabrication. Prepatterned ITO glasses were ultrasonically washed by detergent solution, deionized water, acetone, and ethanol. After washing process, the substrates were dried with compressed N$_2$ flow. The substrates were placed into a UV-Ozone cleaner (Novascan, PSD) for 15 min. Commercial PEDOT: PSS solution (Xi'an Polymer Light Technology Corp Baytron PVP Al 4083) filtered through a 0.45μm N66 filter was spin-coated onto the ITO glass substrates at 3500 rpm for 60s and annealed at 140°C for 10 min. The PEDOT: PSS-coated substrates were swiftly transferred into a glovebox filled with N$_2$. These samples were annealed at 140°C for 5 mins with the N$_2$ flow. Commercial PVK (Xi'an Polymer Light Technology Corp) in chlorobenzene solution (6 mg/mL) was deposited on the PEDOT:PSS layer by spin coating at 2500 rpm for 45 s in a nitrogen-filled glovebox. Then these were annealed at 130 °C for 25 min under the constant N$_2$ flow. Perovskite QDs solution (~15 mg/mL, octane) was spin-coated onto the PVK layer at 2000 rpm for 45 s and then annealed at 90°C for 10 mins. The ZnO nanoparticles ethanol/isopropanol solution (25 mg/mL) was spin-coated onto the QDs layer at 2000 rpm for 45 s and then annealed at 100 °C for 10 mins (Note: This process should

be carried out quickly in order to avoid the degradation of QDs layer caused by ethanol). Finally, Ag electrode (100 nm) was deposited on the ZnO layer by a thermal evaporation system.

Computational Method. In this study, all DFT calculations were carried out using the Vienna Ab initio Simulations Package, VASP (version 5.4.4). The projector-augmented wave method (PAW) was used to describe the ion−electron interaction and the exchange−correlation interaction was described through the generalized gradient approximation (GGA) with the Perdew-Burke−Ernzerhof (PBE) density functional. We have treated the following as valence electrons: Cs(5s5p6s), Pb(5d6s6p), Br(4s4p), Zn(3d4s), C(2s2p), N(2s29) and H(1s). In addition, the kinetic energy cutoff for the plane-wave basis was set at 400 eV. The non-dipolar (010) surface was obtained using METADISE.30 code, where we have added an vacume of 15 Å along z direction and $6 \times 6 \times 6$ and $4 \times 4 \times 1$ centered Monkhorst Pack grids were used for the simulation of the bulk and surface slabs with adsorbates. Especially, in each surface model, there are 8 layers along z direction and we have fixed the 4 bottom layers and allow the rest to relax to mimic the real situation and in this process, the London dispersion interactions was depicted through using the D3 van der Waals correction. All calculations of the bulk and surfaces reactions were performed with the conjugate gradients method with a convergence criterion of 10^{-5} eV and 0.01 eV/Å for the electronic and ionic self-consistence respectively. In addition, to simulate the electroluminescent properties, we have applied an electronic field of 0.5 ev/A in the slab models and meanwhile added a homogeneous background to account for the -2 charged state.

Characterization. All the relevant instruments were same as our previous work. [21] The XRD spectra of QDs were obtained by a MXP21VAHF X-ray diffractometer using Cu Kα radiation ($\lambda = 1.5418$ Å). UV-vis absorption spectra were obtained by a Shimadzu UV-3600 plus spectrophotometer. PL spectra of QDs were obtained by a Gangdong F-280 fluorescence spectrometer. Time-resolved PL decay spectra of QDs were obtained by a Horiba Fluorolog spectrometer coupled with a 375 nm, 45 ps pulsed laser and a time-corrected single-photon counting system. PLQYs were obtained by an integrating sphere (Edinburgh, FLS920). Temperature-dependent photoluminescence spectra measurements were collected using liquid nitrogen in the temperature range of 80-300 K. Transmission electron microscopy (TEM), high-resolution TEM (HRTEM) and Cs-corrected TEM images were performed on a JEOL JEM-

2010 microscope operated at 200 kV and a Tecnai G2 F30 S-TWIN and Titan TM G2 60-300 TEM instrument operated at 300kV. XPS spectra of QDs were tested by a PHI 5000 Versa Probe III spectrometer using a monochromatic Al Kα radiation source (1486.6 eV). FTIR spectra of QDs were obtained by a Varian 3100 FTIR spectrometer. The cross-section view of PeLEDs was obtained by a FIB/ SEM double beam system (FEI, Helios NanoLab 600i). The EL spectra and luminance–current density–voltage curves of PeLEDs were collected by a Keithley 2400 source, a calibrated luminance meter, and a PR-655 Spectra Scan spectrophotometer (Photo Research).

Device characterization. The properties of PeLEDs were performed at room temperature. A Keithley 2400 sourcemeter a calibrated luminance meter, and a PR-655 Spectra Scan spectrophotometer (Photo Research) were used for the measurements. The devices were operated with voltage from 1 V to 10 V with a step voltage of 0.2 V.

Measurement of T_{50} of LED. The time evolution of luminance was measured using the same testing system. Herein, a constant driving current is used for PeLEDs the initial luminance is 115 cd m^{-2} (L_0).

Characterization of the space-charge-limited current (SCLC)

The SCLC measurements were based on the electron-only device of ITO/ZnO/QDs/TPBi/LiF/Al. The current density-voltage (J−V) curves of the devices were collected by using a Keithley 2400 digital source meter under dark condition. The devices were measured in forward scan (-0.05V $\rightarrow$ 2V, step 0.02 V, scan rate: 0.1 V s^{-1}) in an N_2 filled glovebox.

The trap density of the films (n_{trap}) was calculated as:

$$n_{trap} = \frac{2\varepsilon_0\varepsilon V_{TFL}}{eL^2}$$

where e is the elementary charge, and ε, ε_0 and L are the relative dielectric constant, the vacuum permittivity and thickness of the perovskite film, respectively. Here, e is 1.602×10^{-19} C, ε is 23 for CsPbBr$_3$, ε_0 is 8.854×10^{-12} F/m, and L is 30 nm.

The charge carrier mobility (μ) was calculated as:

$$J_D = \frac{9}{8}\varepsilon_0\varepsilon\mu\frac{V^2}{L^3}$$

where J_D, μ and V are current density, the mobility and bias voltage, respectively. The ε, ε_0 and L are the relative dielectric constant, the vacuum permittivity and the thickness of the perovskite film, respectively. ε is 23, ε_0 is 8.854×10^{-12} F/m, and L is 30 nm. The μ were calculated by fitting the slope of $J_D \propto V^2$ in the Chlid's Law stage of SCLC.

Calculation of exciton binding energy (E_b):

The temperature-dependent PL intensity, denoted I(*T*), can be fitted to the Arrhenius equation below:

$$I(T) = \frac{I_0}{1 + A\exp(-\frac{E_b}{K_B T})}$$

in which I_0 is the intensity at 0 K, E_b is the exciton binding energy, and K_B is the Boltzmann constant.

Fitting Model of Exciton–Phonon Coupling Constant:

The evolution of FWHM derived from the broad emission was well-described by the following Fröhlich longitudinal optical phonon broadening mode:

$$\Gamma(T) = \Gamma_0 + \gamma_{ac}T + \frac{\gamma_{LO}}{\exp\left(\frac{E_{LO}}{K_B T}\right) - 1}$$

where Γ 0 was a temperature independent constant related to the scattering from disorder and/or crystallographic imperfections, whose value equaled to the material's FWHM at T=0 K. Γ_{ac} represented the acoustic and longitudinal optical phonon (Fröhlich) interactions and corresponding carrier–phonon coupling constants were γ_{ac} and γ_{LO}, respectively. E_{LO} was the phonon energy.

The calculations of EQE of PeLEDs

The EQE of the QLED was calculated using the following equation:

$$\eta_{EQE} = \frac{C\eta_c\int\lambda I(\lambda)\,d\lambda}{\int I(\lambda)g(\lambda)\,d\lambda}$$

where η_c is the current efficiency of the LED, λ is the wavelength, I(λ) is the EL intensity measured, g(λ) is the photonic response of the human eye at a particular wavelength, and C is

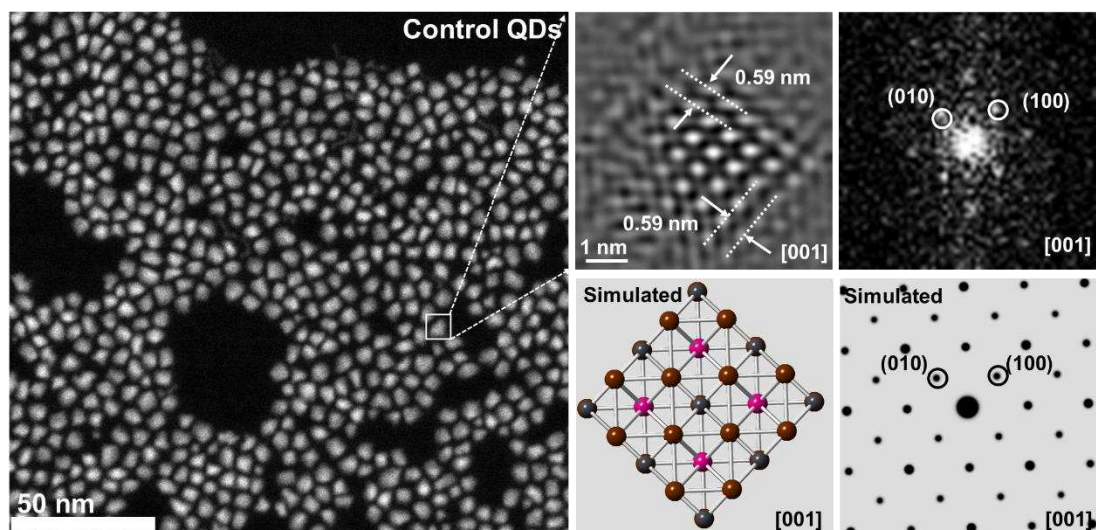a constant that depends on Planck's constant, the velocity of light and the electronic charge.

Figure S1. Low magnification and Atomic-resolution HAADF-STEM images of the control QDs, and their corresponding FFT patterns, which arise from white box area. Simulated crystal structure and FFT patterns of the control QDs.
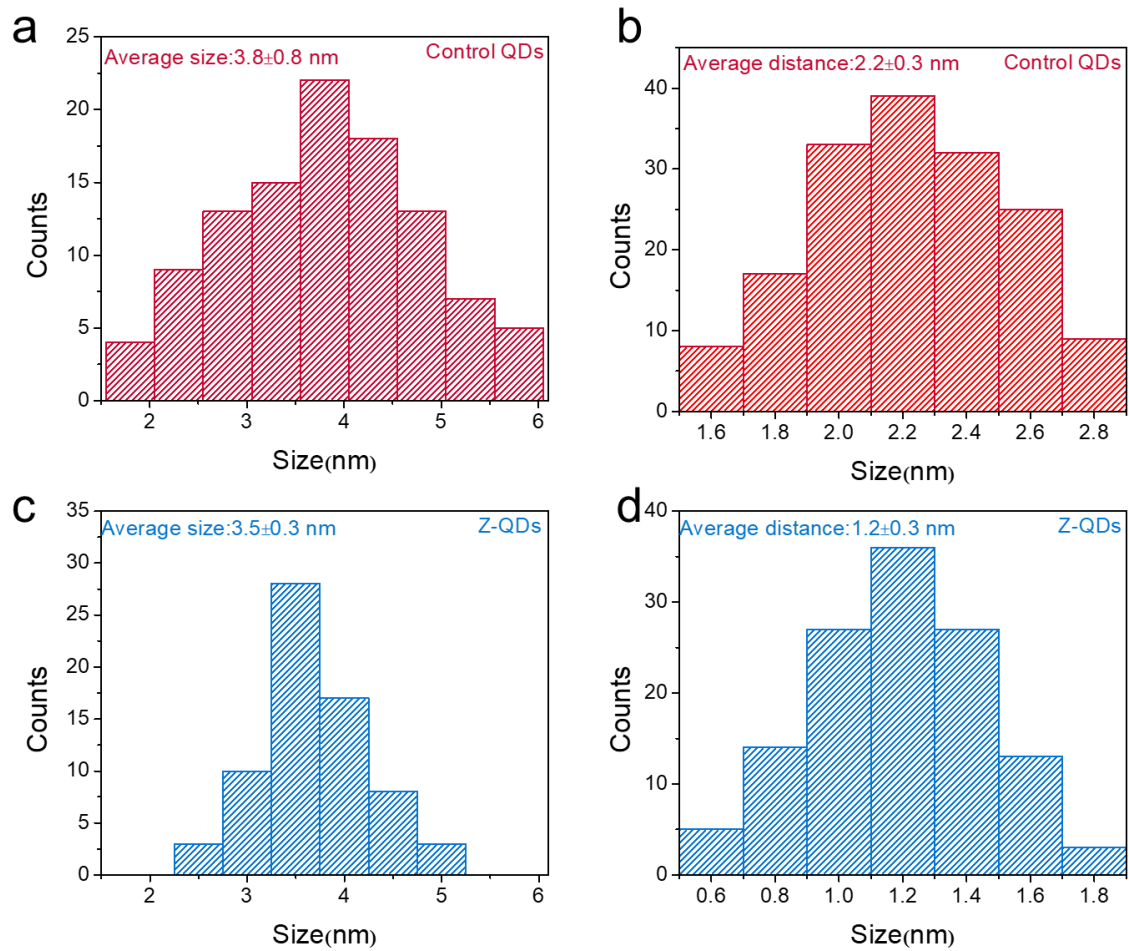
Figure S2. Size distribution histograms of the **(a)** control QDs and **(c)** Z-QDs. Average dot distance histograms of the **(a)** control QDs and **(c)** Z-QDs. The average sizes and distance are calculated assuming that the data approximate to Gaussian distributions.
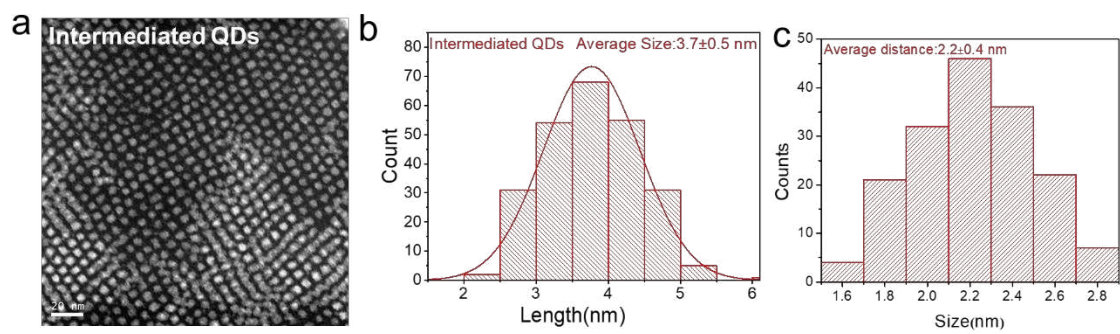
Figure S3. Low magnification HAADF-STEM images, size distribution histograms and average dot distance of the intermediate QDs.
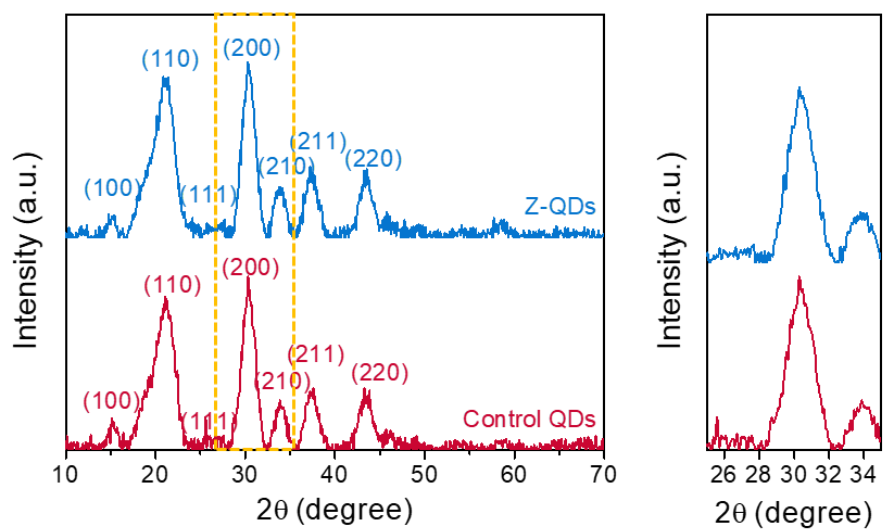
Figure S4. XRD pattern and enlarged-view comparison of the (200) peak position for control QDs and Z-QDs.
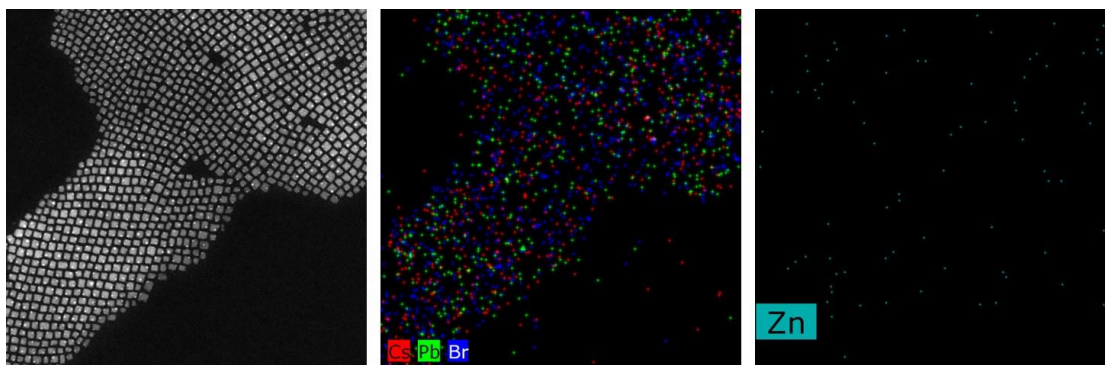
Figure S5. The STEM-HAADF image and EDS mapping of the intermediate QDs. Only noise was detected for Zn.
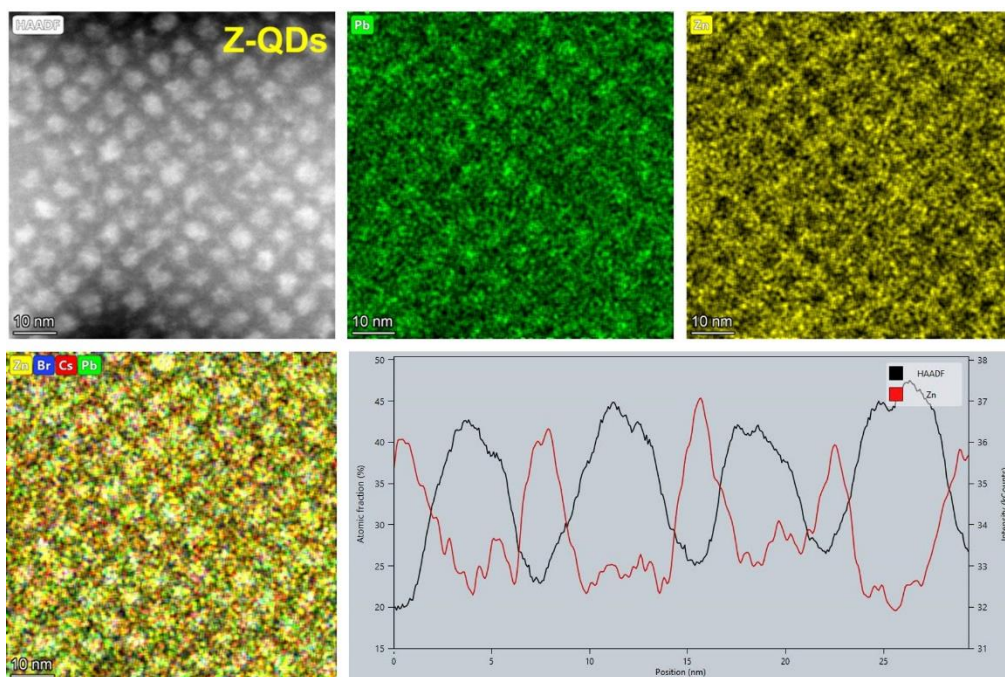
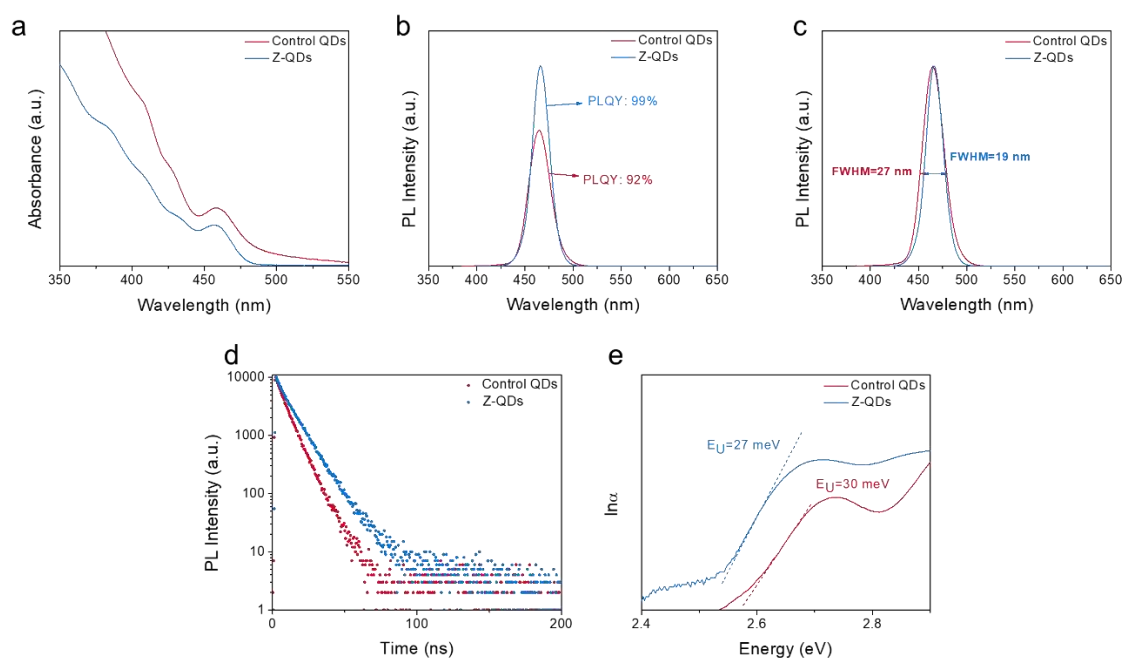**Figure S6.** The STEM-HAADF image and EDS mapping of the Z-QDs.

Figure S7. (a) UV-vis, **(b)** PL, **(c)** Normalized PL, **(d)** time-resoled PL decay spectra and **(e)** Urbach energy diagram for the control QDs and Z-QDs.
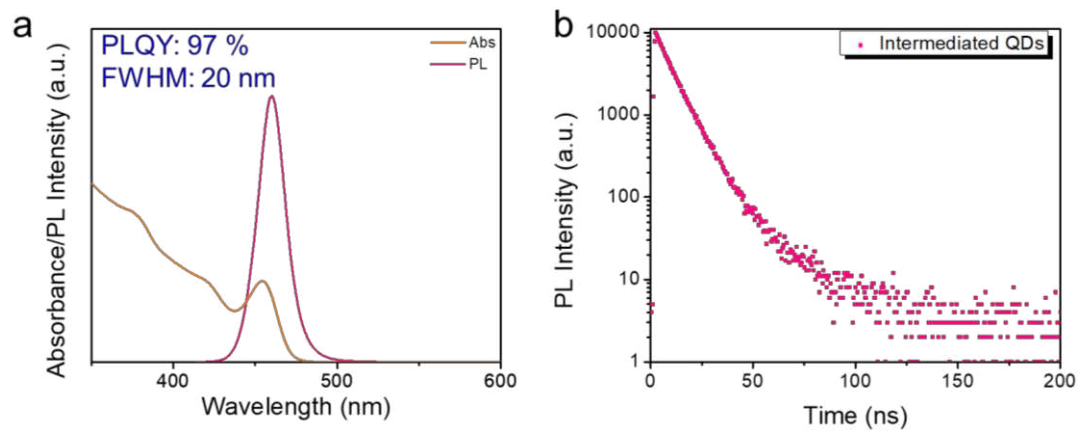
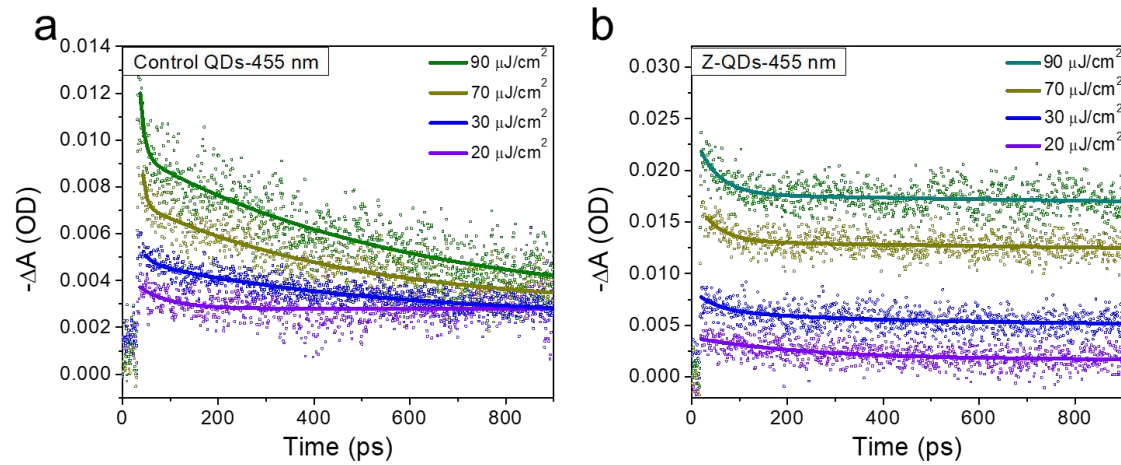**Figure S8.** UV-vis, PL, time-resoled PL decay spectra for intermediated QDs.

Figure S9. Power dependent kinetic traces of **(a)** Control QDs and **(b)** Z-QDs at the exciton bleach.
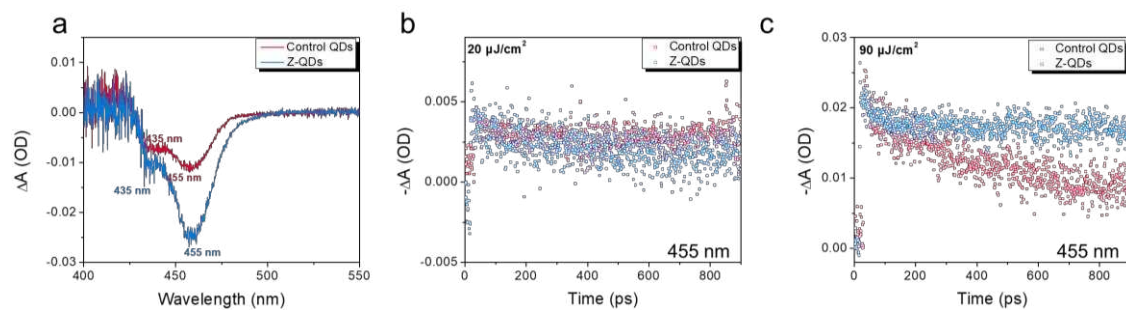
Figure S10. (a) TA spectra of the control QDs and Z-QDs. Comparison of TA bleach recovery kinetics of the **(b)** control QDs and **(c)** the Z-QDs under the monitored wavelength of 455 nm and pulse energy density of 20 μJ/cm^2 and 90 μJ/cm^2.
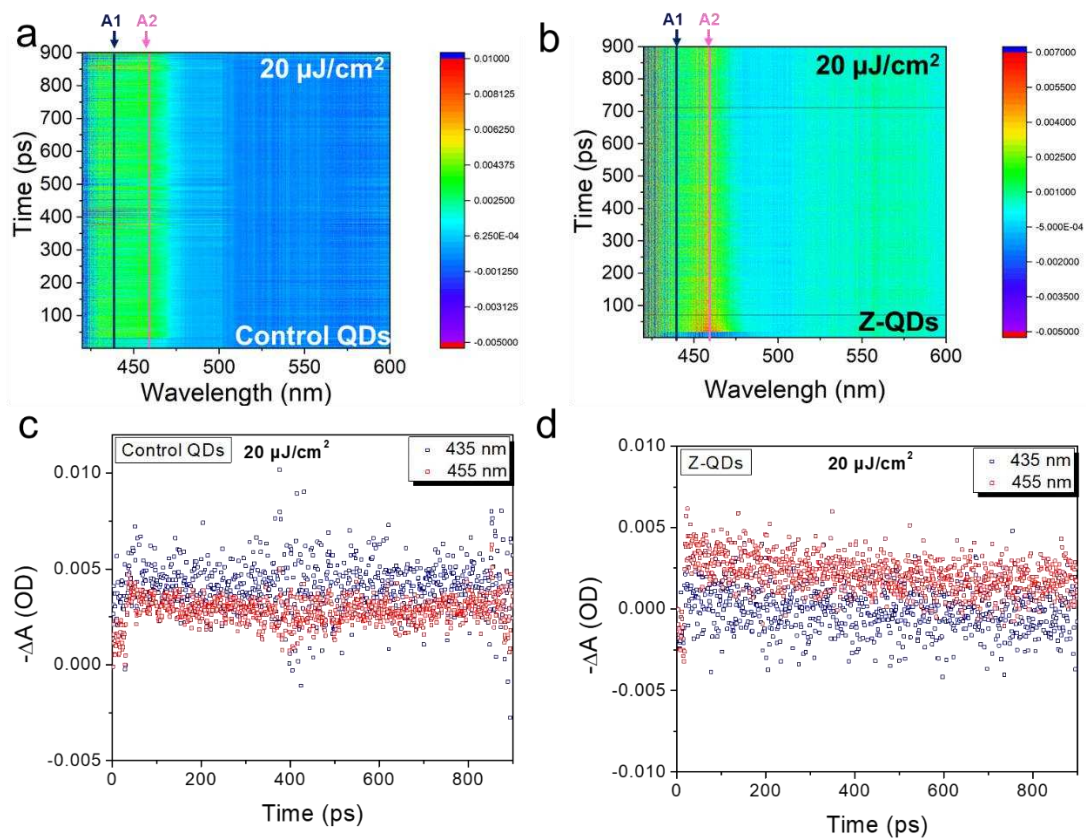
Figure S11. Pseudo color representation of transient absorption (TA) spectra of the **(a)** control QDs and **(b)** Z-QDs. Wavelength of pumping laser=365 nm; pulse energy density ≈ 20 μJ/cm². Comparison of TA bleach recovery kinetics of the **(c)** control QDs and **(d)** the Z-QDs under the pulse energy density of 20 μJ/cm²and the monitored wavelength at 435 nm and 455 nm.
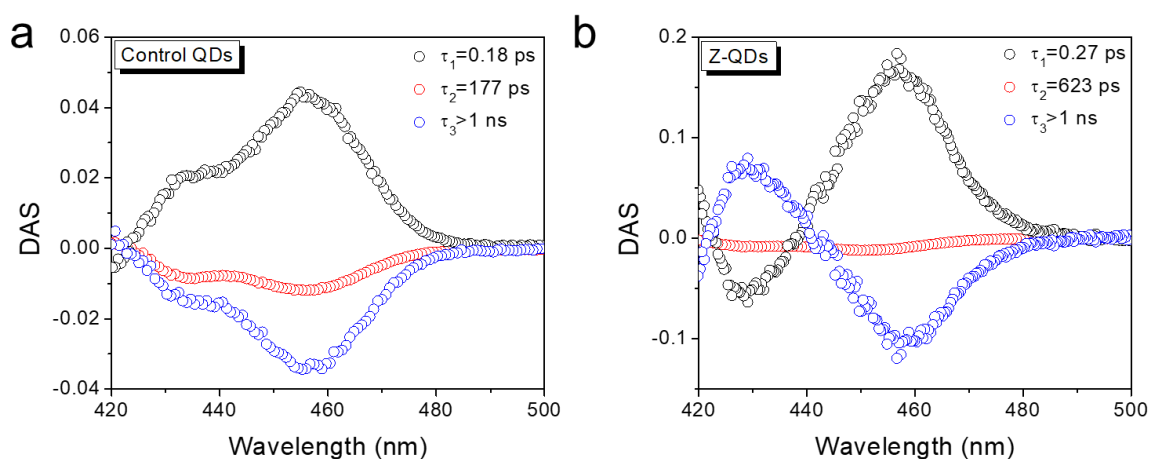
Figure S12. Decay associated spectra (DAS) of the **(a)** control QDs and **(b)** Z-QDs.

The fitted kinetics indicated that the GSB mainly consisted of three photophysical processes, in which the hot electrons relaxed from the excited states to the bottom of the conduction band on the femtosecond time scale: the negative signal is attributed to the hot charge carriers relaxation/stimulated radiation, the positive signal is attributed to the hot carriers absorption. The slightly longer component was attributed to auger recombination and trap-assisted recombination based on the picosecond time scale. The nanosecond components (negative signal) were obviously derived from intrinsic edge exciton radiative recombination and were consistent with the steady-state PL lifetimes. The positive signal is attributed to the photoinduced absorption originated from the lowest excitonic state. Weaker bleaching intensity and longer kinetic time of Z-QDs indicated that Auger recombination was effectively inhibited.
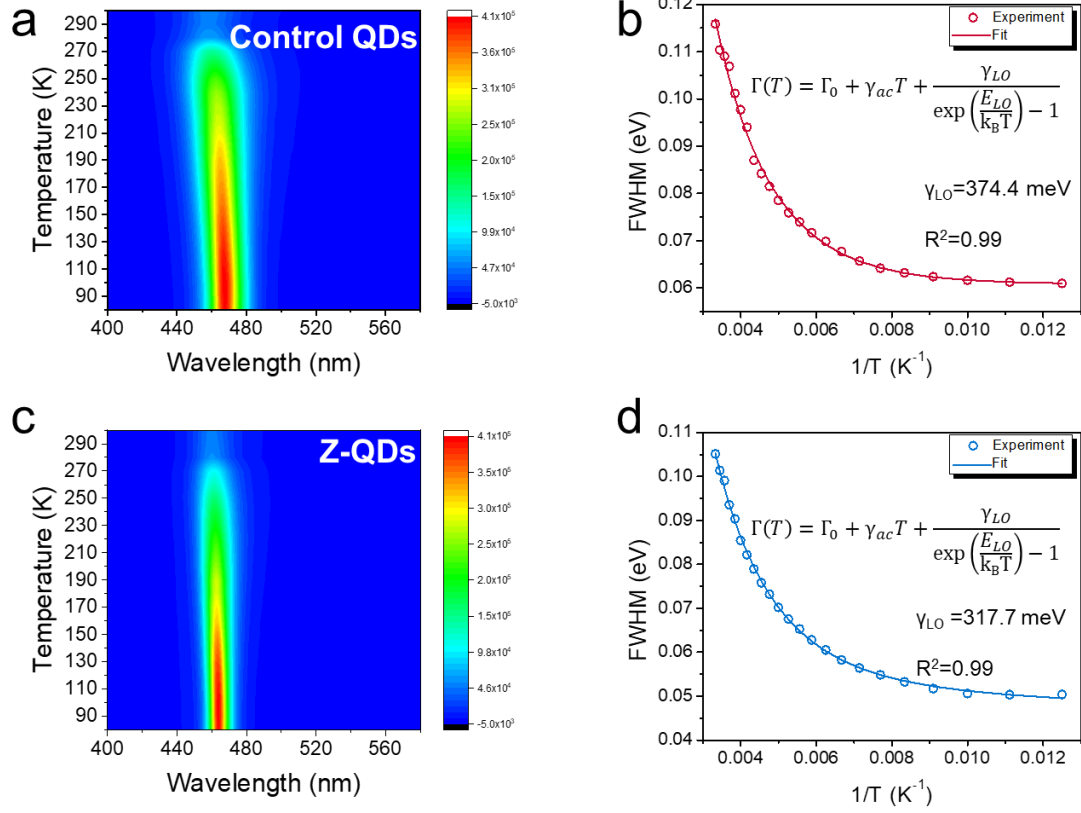
Figure S13. The temperature-dependent PL spectra of the **(a)** control QDs and **(c)** Z-QDs in the range from 80 to 300 K excited at 365 nm. FWHM of the **(b)** control QDs and **(d)** Z-QDs as a function of reciprocal temperature.
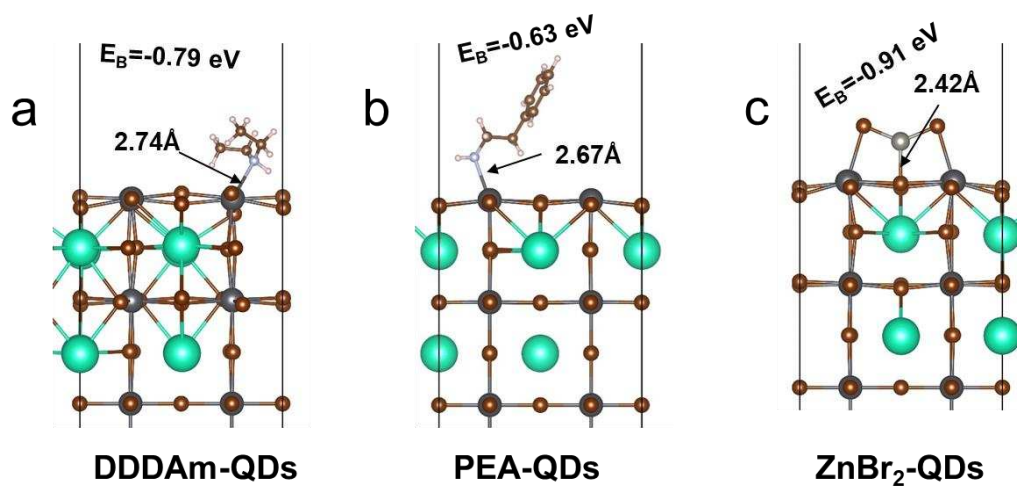
Figure S14. DFT simulated results for binding energy of **(a)** DDDAm, **(b)** PEA and **(c)** ZnBr$_2$ binding with surface of QDs.
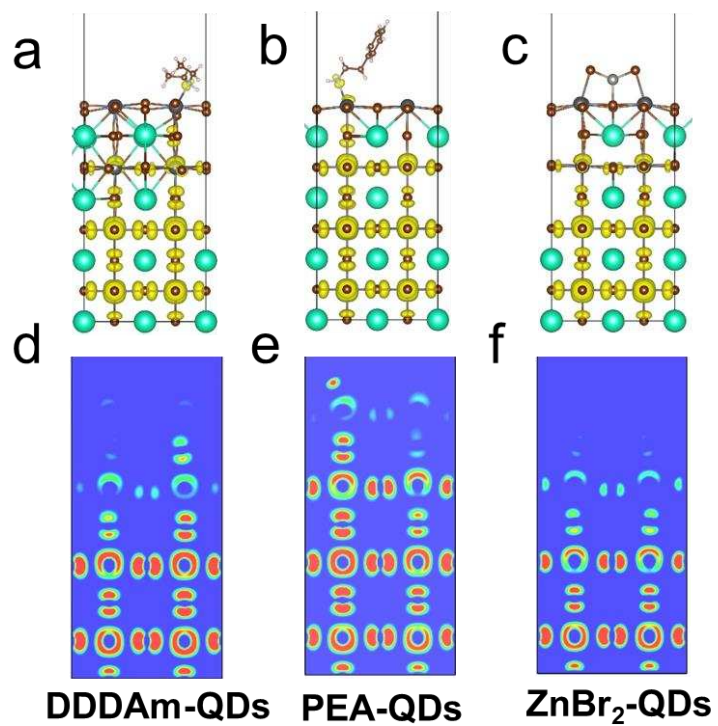
Figure S15. The Partial charge density of the three charged surfaces with a bias of -0.2 eV from VBM and the corresponding 2D plots: DDDAm-QDs (a and d), PEA-QDs (b and e) and $ZnBr_2$ (c and f).
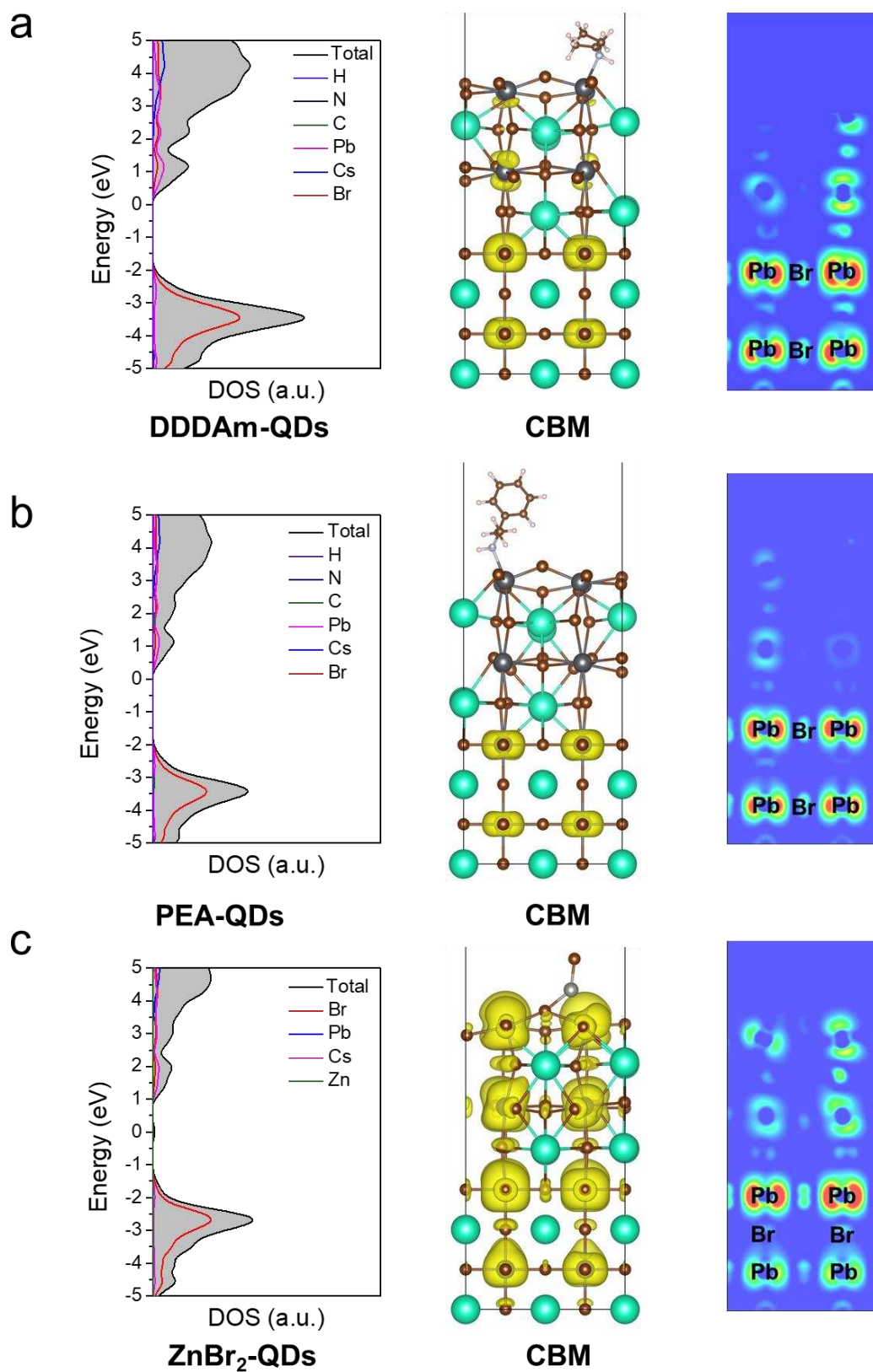
Figure S16. Projected DOS, DFT calculation of electronic charge density with additional two electrons under an external electronic field and corresponding electronic localization function results in the conduction band (yellow) for DDDAm-QDs, PEA-QDs and ZnBr$_2$-QDs.
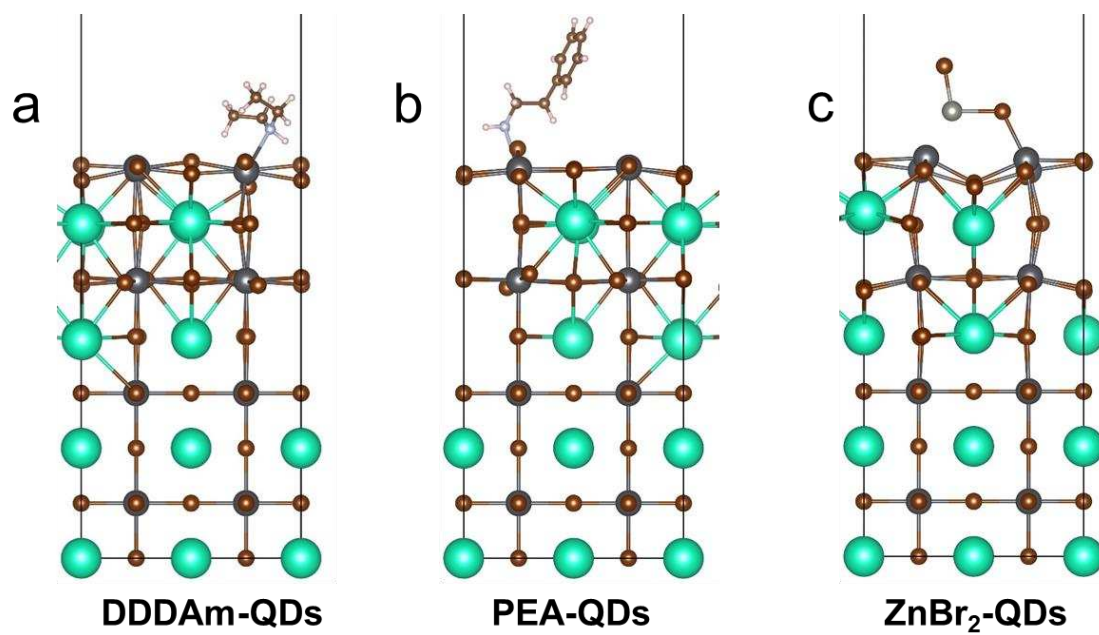
Figure S17. The optimized structures of the surfaces with different adsorbates and additional two electrons under an external electronic field; a): DDDAm; b): PEA; c): $ZnBr_2$.

In this part, we have analyzed the adsorption reactions near the (010) surface, of which the structures with the $ZnBr_2$, PEA and DDDAm adsorbates are shown in **Figure S14**. Out of those three surfaces, we could find that the inorganic ligand $ZnBr_2$ prefers to coordinate with the Br site in the top layer while the PEA and DDDAm tend to move towards the Pb site. In addition, the differences in the binding energy (E_B) and bond distance indicate that it is much cheaper for the $ZnBr_2$ to get coordinated with the surfaces than the other two organic molecules. Then the PDOS and partial charge density near the VBM of the (010) surface with the PEA, DDDAm and $ZnBr_2$ adsorbate is plotted in **Figure S15**. Generally, regarding to the organic absorbate cases (PEA and DDDAm), there is a similar distribution of the density of state, meaning that in both cases, the surfaces after adsorption display a n-type semiconductor where the Fermi level is close to the conduction band maximum (CBM) with a band gap of $\sim$ 1.5 eV to the valence band maximum (VBM) and the electron conduction between VBM and CBM could be activated through the Br-Pb networks inside. While after adsorbing with the inorganic compound ZnBr, a remarkable thing has occurred, which refers to that the Fermi level tends to moves towards the VBM from the CBM, but with a similar distribution of the density of state. Furthermore, no obvious differences in the partial charge density in **Figure S15** demonstrate their similar photoluminescence behaviors, consisted with our experimental records.

To research the electroluminescent properties of the surfaces with adsorption, we then applied an external electronic field (EF) along the z direction with a strength of 0.5 eV/A in the three cases and added two extra electrons in each system to simulate the charged state. The optimized structures can be seen in the **Figure S17** and with a comparison with the neural state without EF, we can see the $ZnBr_2$ ligand tends to move away from the surficial Br site, leaving a Br anion connected with the adjacent Pb site, while no significant changes appear in the organic-adsorbate cases. The related PDOS plots are shown in **Figure S16**, where within our expectation, after the addition of extra electrons, the Fermi level has generally moved cross the VBM for inorganic ligands. Interestingly, the band gap of the system with the $ZnBr_2$ adsorbate declines to 0.9 eV, different from the organic-adsorbate cases (1.8 eV) and another remarkable thing is that the around Fermi level, there is a peak for the Zn orbitals, meaning that it is much probable that the extra electrons prefer to accumulate in the $ZnBr_2$ ligand. To testify this assumption, we finally depicted the partial charge density of the three surfaces in **Figure S16**. For the surfaces with organic adsorbates, the charge density near the CBM and VBM distributes in all the layers from the bottom to the top, while in the surface with $ZnBr_2$, the charge density near the VBM in sub-top and bottom layers has been decreased and instead, a remarkable concentration of the charge around the $ZnBr_2$ molecule is observed, illustrating in a charged state the inorganic adsorbate $ZnBr_2$ could attract the charge in the sub-top layers and concentrate it in the surrounding area.
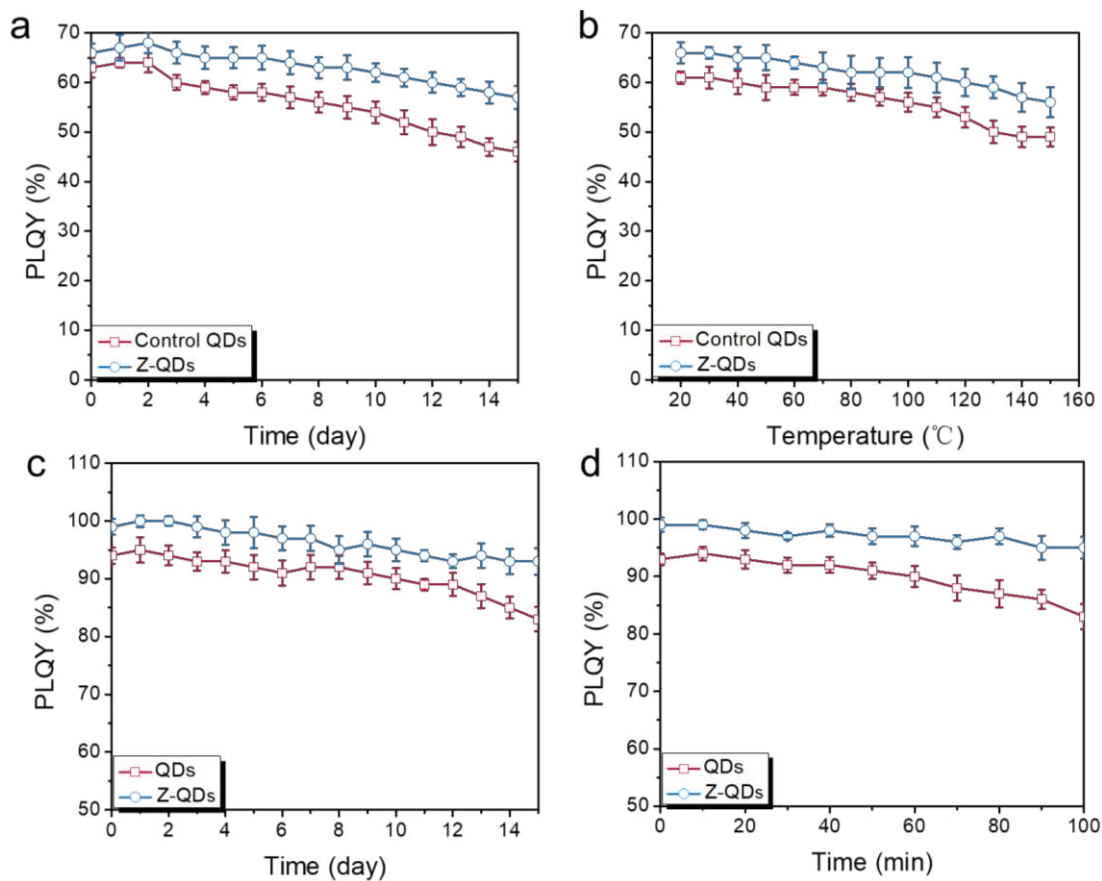
Figure S18. Evolution of PLQYs of control QDs and Z-QDs films after **(a)** different storage time and **(b)** different annealing temperature in ambient (under the average humidity of 60%). **(c)** Evolution of PLQYs of control QDs and Z-QDs solution after different storage time. **(d)** Evolution of PLQYs of control QDs and Z-QDs solution after ultraviolet (UV) irradiation for different times.
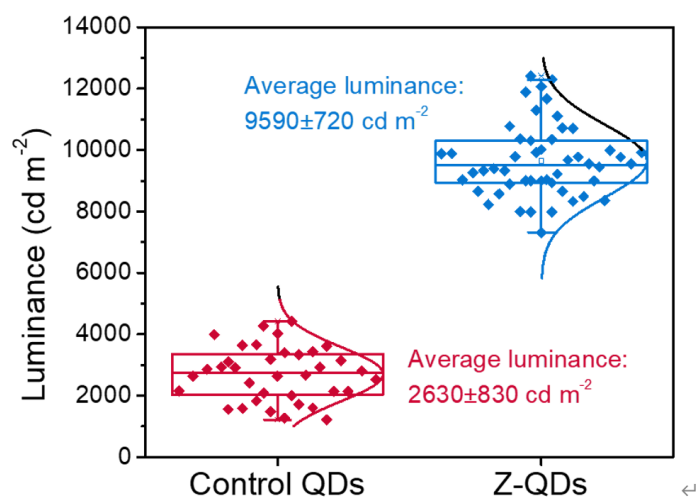
Figure S19. Box plot of the maximum luminance of PeLEDs based on control QDs and Z-QDs.

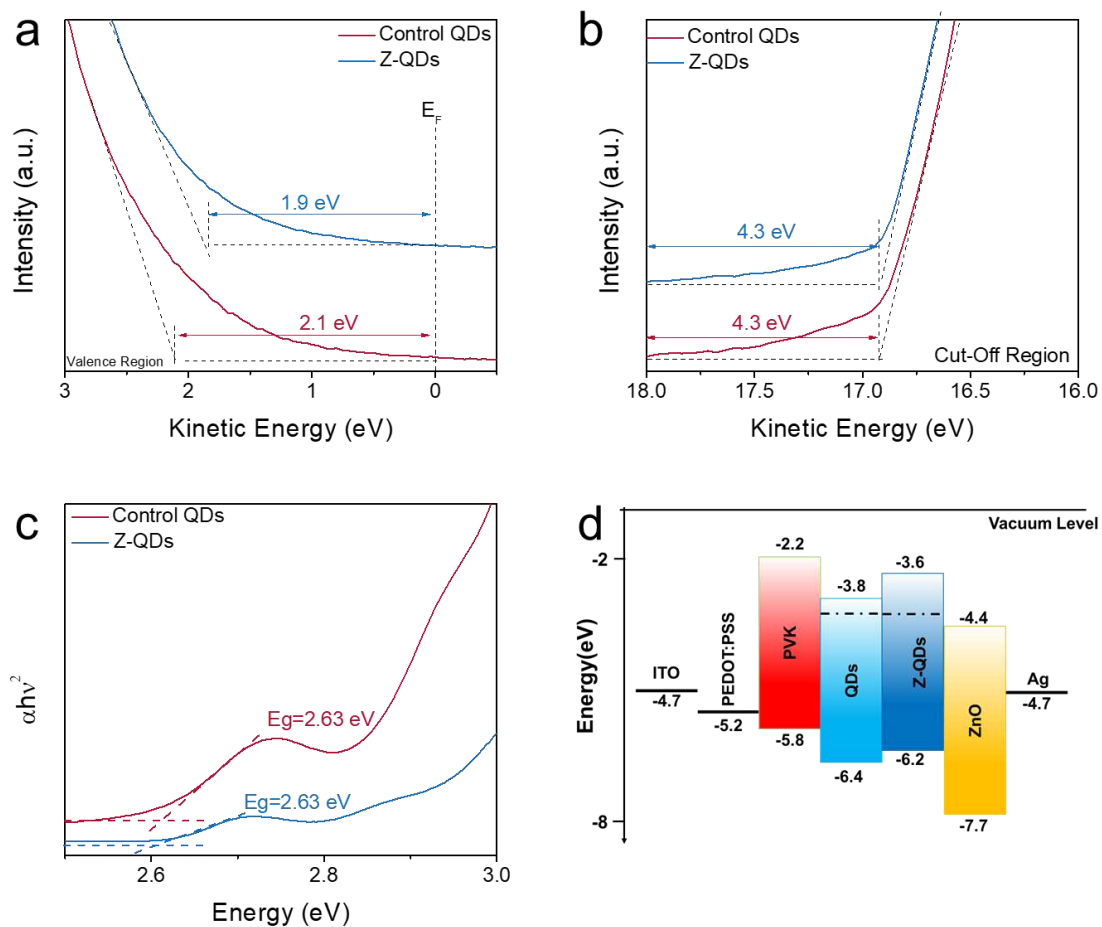**Figure S20.** UPS spectra of the control QDs and Z-QDs: **(a)** cut-off region and **(b)** band-edge region. **(c)** Tauc plots. (d) The energy level alignment for PeLEDs based on control QDs and Z-QDs.

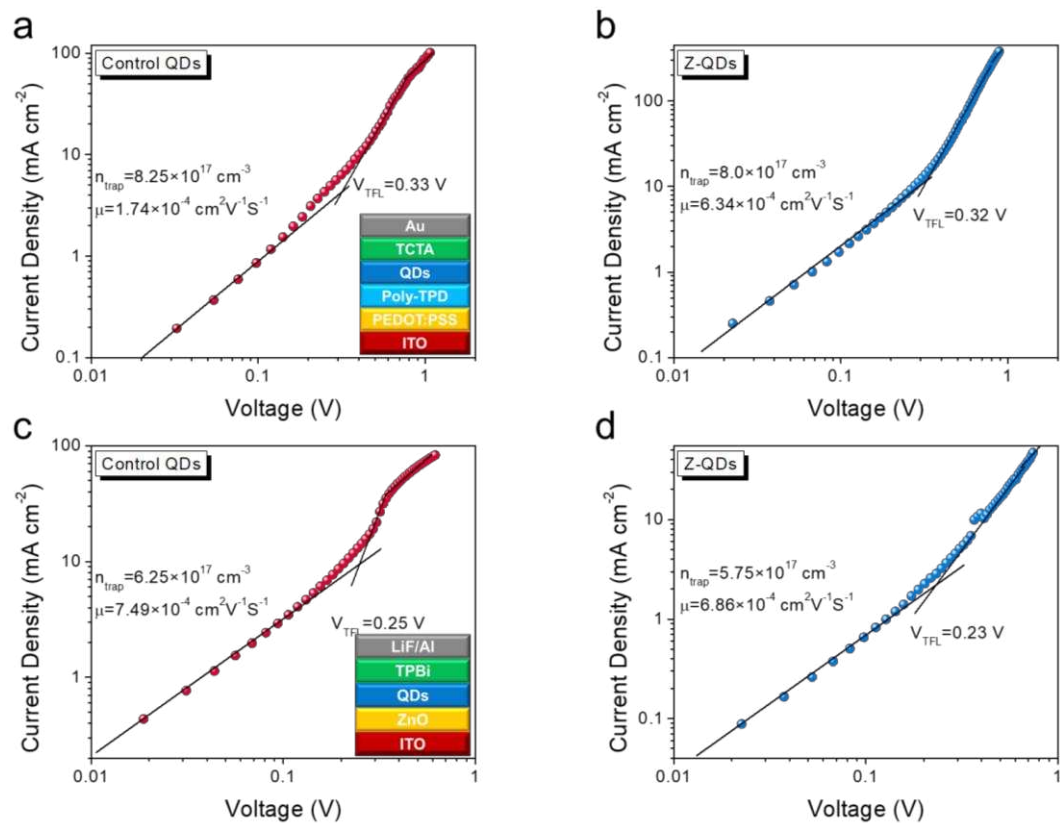**Figure S21.** SCLC patterns of the electron-only devices based on the **(a)** control QDs and **(b)** Z-QDs QDs films. SCLC patterns of the hole-only devices based on the **(c)** control QDs and **(d)** Z-QDs QDs films.
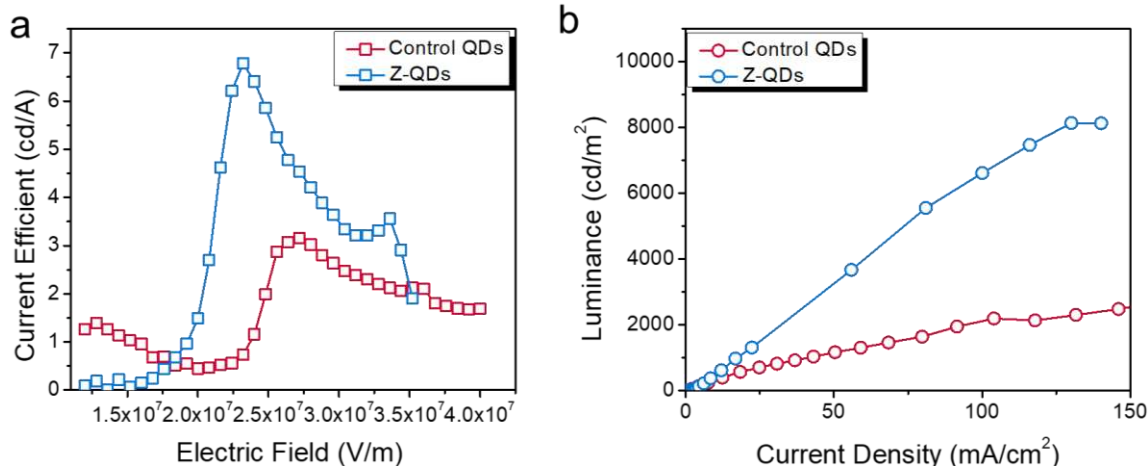
Figure S22. (a) current efficient of PeLEDs versus electric field. **(b)** Luminance of the PeLEDs versus current density.

Ultraviolet photoelectron spectroscopy (UPS) shows that both the CB and VB of the Z-QDs move to higher energies compared with control QDs. The Z-QDs thus exhibit a better energy level alignment, with elimination of the hole injection barrier in LEDs (**Figure S20**); this contributes to the fabrication of high quality PeLEDs using $p-i-n$ structures and helps to balance the transport rates of electrons and holes. According to **Figure S21**, both the calculated electron and hole mobility of the Z-QDs films exhibit the smaller difference between the electron and hole mobilities, indicating the more charge injection balance within the Z-QDs film than that of the control QDs film. In general, there is high carrier density in QDs films under the operated voltage range of PeLEDs, which correspond to the photoexcitation condition with the high pump intensity, Auger recombination is more likely to occur under the electro-excitation condition. Here, we simulate and study the carriers recombination inside QDs films under the electro-excitation condition. As shown in **Figure S22a**, the current efficiency of Z-QDs exhibit the steeper upward trend with the increased electric filed than that of control QDs. The excellent linear curve even at high current density for the PeLED based on the Z-QDs film indicates the less Auger recombination (**Figure S22b**).
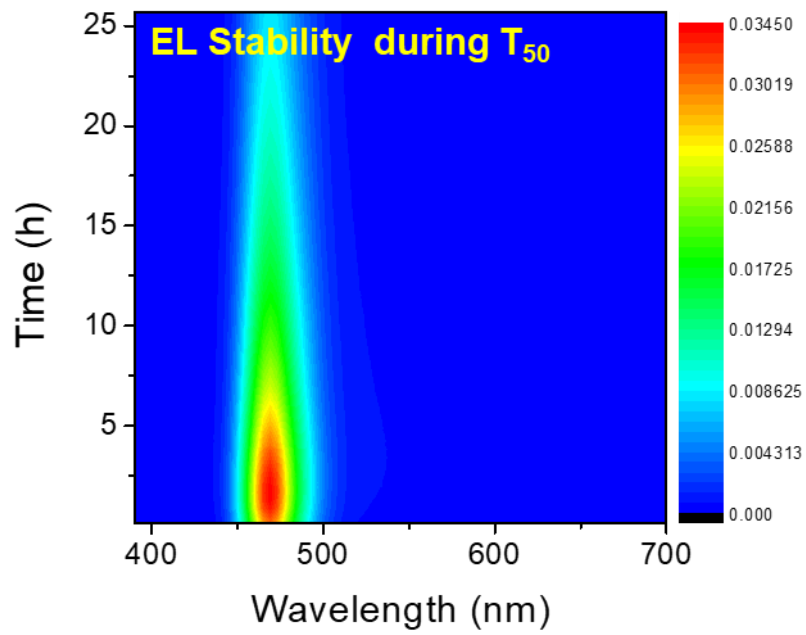
Figure S23. EL spectra with different operational time of the PeLED.

Table S1. Concentration of different elements in Z-QDs calculated from the EDS mapping.

Z	Element	Family	Atomic Fraction (%)	Atomic Error (%)
30	Zn	K	4.17	1.16
35	Br	K	61	10.31
55	Cs	L	15.26	2.38
82	Pb	L	19.58	3.50

Table S2. Concentration of different elements in intermediated QDs calculated from the EDS mapping.

Z	Element	Family	Atomic Fraction (%)	Atomic Error (%)
30	Zn	K	0	0
35	Br	K	60.90	8.80
55	Cs	L	19.30	9.20
82	Pb	L	19.80	15.40

Table S3. Summary of time-resolved PL triexponential fitting parameters for solutions of control QDs and Z-QDs solutions. The deviation of $K_r \times 10^{-2} ns^{-1}$ is calculated when the PL QY with an uncertainty is +/-0.5%; the uncertainty for the lifetimes is +/-0.1ns.

QDs	f_1 [%]	τ_1 [ns]	f_2 [%]	τ_2 [ns]	τ_{ave} [ns]	PLQY [%]	$K_r \times 10^{-2}$ [ns^{-1}]	$K_{nr} \times 10^{-2}$ [ns^{-1}]
Control QDs	9.1	2.1	91.9	10.7	10.1	92	9.1	0.8
Z-QDs	1.1	2.7	98.9	12.3	12.2	99	8.1	0.08

Table S4. Summary of TA spectra fitting parameters for solutions of control QDs and Z-QDs under the pulse energy density of 20 μJ/cm^2.

QDs	f_1 [%]	τ_1 [ps]	f_2 [%]	τ_2 [ps]
Control QDs	2.8	202.2	97.2	6637.2
Z-QDs	2.1	206.1	97.9	6711.0

Table S5. Summary of TA spectra fitting parameters for solutions of control QDs and Z-QDs under the pulse energy density of 90 μJ/cm^2.

QDs	f_1 [%]	τ_1 [ps]	f_2 [%]	τ_2 [ps]
Control QDs	63.3	12.6	36.7	561.7
Z-QDs	7.4	46.9	92.6	5626.0

Table S6. Summary of the typical record performance of pure-blue PeLEDs with emission below 470 nm.

Materials	EL Peak [nm]	Max. Luminance [cd/m^2]	Max.EQE [%]	Operational lifetime	Ref.
CsPb(Cl/Br)$_3$	455	742	0.07	-	1
CsPb(Cl/Br)$_3$	470	350	0.07	Spectra shift at ~15 s	2
CsPb(Cl/Br)$_3$	469	111	0.5	T_{50} =1 s @ 1 mA cm^{-2}	3
Mn-CsPb(Cl/Br)$_3$	466	245	2.12	T_{50} =1 s @ 1 mA cm^{-2}	4
CsPb(Cl/Br)$_3$	461	763	0.8	-	5
Ni-CsPb(Cl/Br)$_3$	460	33	1.35	T_{50} =51.5 s @ 3.7 V	6
PEA-CsPb(Cl/Br)$_3$	470	620	2.12	T_{50} =24 s @ 7 V	7
Ni-CsPb(Cl/Br)$_3$	470	612	2.4	-	8
CsPbBr$_3$	470	3850	4.7	T_{50} =12 h@102cd/m^2	9
CsPbBr$_3$	469	10410	5.0	T_{50} =59 h@100cd/m^2 T_{50} =80 min@1700cd/m^2	10
Rb$^+$-Li$^+$-CsPbSrBr$_3$	467	510	1.43	T_{50} =140 s@140cd/m^2	11
Cs$_{0.8}$Rb$_{0.2}$Pb$_{0.95}$Ni$_{0.05}$Br$_{1.8}$Cl$_{1.2}$	467	~200	2.14	-	12
PPDA-PEA-CsPbBr$_3$	465	211	2.6	T_{50} =13.5 min@0.35mA/cm^2	13
CsPb(Br$_x$Cl$_{1-x}$)$_3$	461	318	1.4	-	14
POEA-CsPbBr$_{1.65}$Cl$_{1.35}$	468	122.1	0.71	-	15
CsPb(Br$_x$Cl$_{1-x}$)$_3$	470	465	6.3	T_{50} =99 s @ 4.5 V	16
CsPbBr$_3$	469	12060	10.3	T_{50} =25 h@115cd/m^2	This Work

Reference

(1) Song, J.; Li, J.; Li, X.; Xu, L.; Dong, Y.; Zeng, H. Quantum Dot Light-Emitting Diodes Based on Inorganic Perovskite Cesium Lead Halides ($CsPbX_3$). Adv. Mater. **2015**, 27 (44), 7162-7167.

(2) Yao, E. P.; Yang, Z.; Meng, L.; Sun, P.; Dong, S.; Yang, Y.; Yang, Y. High-Brightness Blue and White LEDs based on Inorganic Perovskite Nanocrystals and their Composites. Adv. Mater. **2017**, 29 (23), 1606859.

(3) Gangishetty, M. K.; Hou, S.; Quan, Q.; Congreve, D. N. Reducing Architecture Limitations for Efficient Blue Perovskite Light-Emitting Diodes. Adv. Mater. **2018,** 30 (20), 1706226.

(4) Hou, S.; Gangishetty, M. K.; Quan, Q.; Congreve, D. N. Efficient Blue and White Perovskite Light-Emitting Diodes via Manganese Doping. Joule 2018, 2 (11), 2421-2433.

(5) Yang, D.; Li, X.; Wu, Y.; Wei, C.; Qin, Z.; Zhang, C.; Sun, Z.; Li, Y.; Wang, Y.; Zeng, H. Surface Halogen Compensation for Robust Performance Enhancements of $CsPbX_3$ Perovskite Quantum Dots. Adv. Opt. Mater. **2019**, 7 (11), 1900276.

(6) Zhang, B.; Yuan, S.; Ma, J.; et al. General Mild Reaction Creates Highly Luminescent Organic-Ligand-Lacking Halide Perovskite Nanocrystals for Efficient Light-Emitting Diodes. J. Am. Chem. Soc. **2019**, 141, 15423-25432.

(7) Shao, H.; Zhai, Y.; Wu, X.; Xu, W.; Xu, L; Dong, B.; Bai, X.; Cui, H.; Song, H., High brightness blue light-emitting diodes based on $CsPb(Cl/Br)_3$ perovskite QDs with phenethylammonium chloride passivation. Nanoscale **2020**, 12, 11728-11734.

(8) Pan, G.; Bai, X.; Xu, W.; Chen, X.; Zhai, Y.; Zhu, J.; Shao, H.; Ding, N.; Xu, L.; Dong, B.; Mao, Y.; Song, H., Bright Blue Light Emission of $Ni^{(2+)}$ Ion-Doped $CsPbCl_xBr_{3-x}$ Perovskite Quantum Dots Enabling Efficient Light-Emitting Devices. ACS Appl. Mater. Interfaces **2020,** 12 (12), 14195-14202.

(9). Bi, C.; Yao, Z.; Sun, X.; Wei, X.; Wang, J.; Tian, J., Perovskite Quantum Dots with Ultralow Trap Density by Acid Etching-Driven Ligand Exchange for High Luminance and Stable Pure-Blue Light-Emitting Diodes. Adv. Mater. **2021**, 33 (15), e2006722.

(10). Yao, Z.; Bi, C.; Liu, A.; Zhang, M.; Tian, J., High brightness and stability pure-blue perovskite light-emitting diodes based on a novel structural quantum-dot film. Nano Energy **2022**, 95, 106974.

(11) Cai, L.; Liang, D.; Wang, X.; Zou, Y.; Song, T.; Sun, B. Efficient and Bright Pure-Blue All-Inorganic Perovskite Light-Emitting Diodes from an Ecofriendly Alloy. J. Phy. Chem. Lett. **2021**, 12, 1747.

(12) Pan, J.; Zhao, Z.; Fang, F.; Wang, L.; Wang, G.; Liu, C.; Chen, J.; Xie, J.; Sun, J.; Wang, K.; et al. Multiple Cations Enhanced Defect Passivation of Blue Perovskite Quantum Dots Enabling Efficient Light-Emitting Diodes. Adv. Opt. Mater. **2020**, 8, 2001494.

(13) Yuan, S.; Wang, Z.-K.; Xiao, L.-X.; Zhang, C.-F.; Yang, S.-Y.; Chen, B.-B.; Ge, H.-T.; Tian, Q.-S.; Jin, Y.; Liao, L.-S. Optimization of Low-Dimensional Components of Quasi-2D Perovskite Films for Deep-Blue Light-Emitting Diodes. Adv. Mater. **2019**, 31, 1904319.

(14) Ochsenbein, S. T.; Krieg, F.; Shynkarenko, Y.; Rainò, G.; Kovalenko, M. V. Engineering Color-Stable Blue Light-Emitting Diodes with Lead Halide Perovskite Nanocrystals. ACS Appl. Mater. Interfaces **2019**, 11, 21655.

(15) Tan, Z.; Luo, J.; Yang, L.; Li, X.; Deng, Z.; Gao, L.; Chen, H.; Li, J.; Du, P.; Niu, G.; et al. Spectrally Stable Ultra-Pure Blue Perovskite Light-Emitting Diodes Boosted by Square-Wave

Alternating Voltage. Adv. Opt. Mater. **2020**, 8, 1901094.

(16) Zheng, X.; Yuan, S.; Liu, J.; Yin, J.; et al, Chlorine Vacancy Passivation in Mixed Halide Perovskite Quantum Dots by Organic Pseudohalides Enables Efficient Rec. 2020 Blue Light-Emitting Diodes. ACS Energy Lett. **2020**, 5 793-798.